Reversible and non-volatile metal-to-insulator chemical transition in molybdenum oxide films

YAEL GUTIÉRREZ,[1,*] ◉ GONZALO SANTOS,[2] FABIO PALUMBO,[1] MIRCEA MODREANU,[3,5] FERNANDO MORENO,[2] ◉ AND MARIA LOSURDO[4]

[1]*Institute of Nanotechnology, CNR-NANOTEC, via Orabona 4, 70126 Bari, Italy*
[2]*Departamento de Física Aplicada, Universidad de Cantabria, Avda. Los Castros s/n 39005 Santander, Spain*
[3]*Tyndall National Institute, University College Cork, T12 R5CP Cork, Ireland*
[4]*Istituto di Chimica della Materia Condensata e delle Tecnologie per l'Energia, CNR-ICMATE, C.so Stati Uniti 4, 35127 Padova, Italy*
[5]*mircea.modreanu@tyndall.ie*
[*]*yael.gutierrezvela@nanotec.cnr.it*

Abstract: Significant effort is being dedicated to developing alternative materials whose optical properties can be controllably and reversibly modified. Here, we experimentally demonstrate the reversible non-volatile molybdenum oxides MoO_3-to-MoO_2 transition associated to a change from a metallic to a dielectric behavior through cycles of thermal annealing in air and hydrogen (H_2). A full cycle is demonstrated by characterizing structurally and optically the transition using Raman spectroscopy and spectroscopic ellipsometry. The potential applicability of the metal-to-insulator transition in MoO_x is benchmarked through comparison with a canonical Mott insulator VO_2 in a reconfigurable reflective configuration as well as in cladded waveguide schemes.

1. Introduction

Optical devices with a reconfigurable response are in focus of ongoing photonic developments. At the basis of this research field is the study of novel materials whose optical properties can be modulated through external stimuli. In the last years, vanadium dioxide (VO_2), which shows large modification in physical properties (e.g., refractive index, electrical resistivity) upon external excitation, has been of interest because of its insulator-to-metal transition (IMT) that can be induced by thermal heating (above $T_c = 68°C$), applied electric fields ($E = 10^5$ V/cm), injected carrier density ($n_e = 10^{18}$ cm^{-3}) and optical pulses [1]. The IMT in VO_2 leads to a volatile metallic state that, when external excitations are switched off, disappears bringing reversibly back VO_2 to its insulating state. The large refractive modulation appearing during this process has been proven in applications related to reconfigurable antennas/metasurfaces [2,3], amplitude modulators integrated in waveguides [4–6], as well as in the dynamic modulation of spontaneous light emission [7–9], among others [1]. Although VO_2 shows a large-refractive-index modulation, it also exhibits large extinction coefficient in the visible and near-IR, which directly correlates with undesirable optical losses in photonic devices.

Nevertheless, abrupt changes in electronic and optical properties can also be induced in transition metal oxides by tuning the oxidation states in the transition metal. For instance, molybdenum oxides, MoO_x, can exist in a wide variety of different stoichiometric and non-stoichiometric phases due to the multiple valence states of molybdenum ranging from +3 to +6. Among all molybdenum oxides, MoO_3 is of special interest due to its wide band gap semiconducting behavior with reported experimental value of the energy band gap of ≈ 3.0 eV [10]. MoO_3 is a van der Waals semiconductor with an orthorhombic crystal lattice consisting of

double layers of MoO_6 octahedra as a framework, and recently is receiving significant attention due to its ability to support highly anisotropic phonon polaritons (PhPs)—infrared (IR) light coupled to lattice vibrations—offering an unprecedented platform for controlling the flow of energy at the nanoscale [11,12]. Conversely, MoO_2 crystallizes in a distorted rutile structure and presents a metallic band structure. Its metallicity arises from the presence of Mo 4d orbitals near the Fermi level [13]. The metallicity of MoO_2 has already been exploited to generate localized surface plasmon resonances (LSPRs) for surface-enhanced Raman spectroscopy (SERS) applications [13,14] as well as electrode material for applications such as dynamic random-access memory (DRAM) capacitors and lithium ion batteries [15–18]. Therefore, the MoO_3-to-MoO_2 transition enables an insulator-to-metal transition with the advantage of low-loss behavior of MoO_3 in the visible and near-IR spectral region and a non-volatile character. This peculiarities are being exploited in the design of switchable reflective primary color subpixels for application in non-volatile displays based on the MoO_3-to-MoO_2 transition [19,20].

In this work, we experimentally demonstrate the reversible non-volatile MoO_3-to-MoO_2 transition reporting a change from a metallic to a dielectric behavior in the dielectric function. The MoO_3-to-MoO_2 transition has been achieved through cycles of thermal annealing in air and hydrogen (H_2) and monitored structurally by Raman spectroscopy. The change of the dielectric function from insulating MoO_3 to metallic MoO_2 is probed by spectroscopic ellipsometry, from which we derived the refractive index contrast as key metric for the benchmarking of molybdenum oxide for reconfigurable photonics applications.

2. Methods

2.1. Sample fabrication

Amorphous MoO_3 films were deposited at room temperature by e-beam evaporation using MoO_3 pellets (Pi-KEM 99.99% purity) in a Leybold SYRUS pro 710 on 4-inch Si (100) and 40 nm Pt/5nm Ti/Si (100) substrates in the same run. The nominal thickness of the films was 150 nm and 170 nm. The Si (100) wafers were cleaned prior the deposition using a standard RCA cleaning procedure. The 40nm Pt/5nmTi metal stack was grown by sputtering in a TEMESCAL using Ti and Pt sputtering targets.

The crystallization of the samples was performed by thermal annealing of the films at T= 400°C in air or in H_2 with a pressure of 100 mbar.

2.2. Structural and chemical characterization

Films, both as deposited and after annealing cycles, were characterized structurally by Raman spectroscopy (LabRam Horiba set up using a ×100 microscope objective (NA = 0.9) and excitation wavelength of 532 nm) as MoO_2 and MoO_3 assume different crystalline symmetry groups and Raman selection rules gives different Raman active phonon modes that are unique and specific for the MoO_3 orthorhombic structure and MoO_2 rutile structure

The stoichiometry of the as-deposited amorphous and crystallized films was checked by X-ray photoelectron spectroscopy (XPS) measurements carried out by a Scanning XPS Microprobe (PHI 5000 Versa Probe II, Physical Electronics) equipped with a monochromatic Al Kα x-ray source (1486.6 eV), with a spot size of 200 μm. Survey (0–1200 eV) and high-resolution spectra were acquired in fixed analyzer transmission (FTA) mode at a pass energy of 117.40 and 29.35 eV, respectively, and at a take-off angle of 45° with respect to the sample surface. Surface charging was compensated using a dual beam charge neutralization system, and the hydrocarbon component of C1s spectrum was used as internal standard for charging correction, and it was fixed at 284.5 eV.

2.3. Optical characterization

Optical properties, namely spectra of the complex pseudodielectric function, $\langle \epsilon \rangle = \langle \epsilon_1 \rangle + i \langle \epsilon_2 \rangle$, were measured by spectroscopic ellipsometry (UVISEL Horiba) in the photon energy range 0.75–6.5 eV with a resolution of 0.05 eV with an angle of incidence of 70°. The ellipsometry measurements were fit to a three-media substrate/film/air model, where the Si and Pt substrates were experimentally measured prior deposition of MoO_x films. The MoO_3 layer was parameterized using the Tauc–Lorentz oscillator model and MoO_2 with a Tauc–Lorentz oscillator model plus a Drude term [21]. The experimental reflection spectra at 70° were also measured by spectroscopic ellipsometry.

2.4. Reflectance and colorimetry calculations

The reflectance of the multilayer structure was calculated using the Transfer Matrix Method (TMM). TMM allows to calculate the reflectance spectrum of an arbitrary system of homogeneous and non-magnetic multilayers by establishing conditions for the electric field along the boundary of two consecutive media [22].

Reflective color was calculated from experimental and theoretical reflectance spectra. The resulting color also depends on the illuminant and observer. All the color simulations presented here assume standard D65 illuminant and a CIE standard observer. Illuminant D65 corresponds to average daylight, and CIE standard observer represents mean human spectral sensitivity to visible spectrum range [23]. In this paper, CIE1931 space has been chosen because is one of the most accepted to study the resulting color by the reflective displays. The color difference (ΔE) has been quantified using the *Lab* color space as

$$\Delta E = \sqrt{(a_1 - a_2)^2 + (b_1 - b_2)^2 + (L_1 - L_2)^2} \tag{1}$$

2.5. Calculation of transmission through cladded Si_3N_4 waveguides

Finite-difference time-domain (FDTD) simulations were performed with Ansys Lumerical. The simulated geometry consists of a silicon nitride (Si_3N_4) waveguide (width = 800 nm and height = 300 nm) on a SiO_2 substrate with a MoO_x or VO_2 patch on top of thickness 20 nm and variable length (see Fig. 5(a)). In the FDTD simulation region, a MODE source is used to inject a guided mode (wavelength λ = 1550 nm) into the waveguide inside the simulation region. From a list of possible modes, the TE mode is selected for injection.

3. Results

3.1. Reversible MoO_3-to-MoO_2 transition

Figure 1 summarizes the processing path to the reversible MoO_3-to-MoO_2 transition starting from MoO_{3-x} films grown by e-beam deposition on Si and Pt substrates. After each processing step, the sample was structurally and optically characterized by Raman spectroscopy and spectroscopic ellipsometry. The steps followed to prove the reversible MoO_3-to-MoO_2 transition are as follows:

1. The starting point of experiments consist of 150 nm and 170 nm thick MoO_{3-x} films deposited on Si and Pt substrates. The as deposited films are amorphous as revealed by the absence of peaks in the Raman spectrum as shown in Fig. 1(b). The peaks visible in the Raman spectra at 300 and 520 cm^{-1} are assigned to the Si substrate.

2. After annealing in air at 400°C, the film is crystallized MoO_3 as it fully oxidizes following the chemical reaction $MoO_x + (3\text{-}x)/2\ O_2 \rightarrow MoO_3$. This is corroborated by the Raman spectrum in Fig. 1(b), which shows Raman bands at 116, 128, 158, 198, 217, 245, 283, 337, 365, 378, 471, 666, 819 and 995 cm^{-1} ascribed to MoO_3 [24]. The annealing process

from amorphous MoO_x to crystalline MoO_3 entails a change in the optical properties of the film as revealed by the change in the imaginary part, $\langle \epsilon_2 \rangle$, of the pseudo dielectric ($\langle \epsilon \rangle = \langle \epsilon_1 \rangle + i \langle \epsilon_2 \rangle$) function in Fig. 1(d).

3. Subsequently, the sample was annealed in H_2 at 400°C. Upon reduction in H_2, the Raman spectrum changed, as shown in Fig. 1(c), revealing peaks at 201, 205, 227, 343, 350, 360, 422, 455, 466, 493, 567, 582 and 737 cm^{-1} consistent with MoO_2 [25]. The thermal annealing in H_2 involves the thermal activation of the oxygen desorption according to the reaction $MoO_3 + H_2 \rightarrow MoO_2 + H_2O$. This chemical reduction of MoO_3-to-MoO_2 accompanies with a change in $\langle \epsilon_2 \rangle$ as reported in Fig. 1(d). The change in $\langle \epsilon_1 \rangle$ is shown in Figure S1. Furthermore, from ellipsometry analysis of a MoO_3 film (initial thickness 170 nm) before and after the H_2 annealing, a $\approx$ 10 nm (or 6%) expansion of the thickness of the film can be found.

4. In order to show a complete cycle and reversibility of the MoO_3-to-MoO_2 transition, the sample was again annealed in air. The Raman spectrum after this process is consistent with the complete transformation of MoO_2 into MoO_3 as shown in Fig. 1(c), according to the reaction $MoO_2 + O_2 \rightarrow MoO_3$. The reversibility of the process is also visible in the $\langle \epsilon_2 \rangle$ spectrum of Fig. 1(d), which matches that of the MoO_3 film before its reduction to MoO_2 in step #3. Similar behavior is seen in $\langle \epsilon_1 \rangle$ as shown in Figure S1.

Interestingly, we have verified that the switched state, MoO_2 and/or MoO_3 are stable up to 6 months after the H_2 annealing of the MoO_3 starting point through repeated spectroscopic ellipsometry measurements in time.

The metal-to-insulator transition that entails the MoO_3-to-MoO_2 reversible transformation can also be inferred in the valence band analysis by XPS in Fig. 1(e), showing semiconducting high bandgap MoO_3 after annealing in air and metallic states populating the region around the 0 eV (i.e. Fermi level) up to BE of 2 eV for the MoO_2 obtained by annealing in H_2. The peaks appearing in the XPS valence band spectra at 0.5 and 1.45 eV are in good agreement with values reported in literature (0.60 and 1.60 eV experimental values and 0.50 and 1.35 eV computed values) [26] and are assigned to Mo 4d bands. These peaks are associated with σ- and π-bonding states which are responsible for the metallic behavior of this oxide. In particular, the π bonding is not strong enough to split the $t_{\perp}$ (π) bands off completely from the rest of the unoccupied Mo 4d bands to give an insulating character to the material [26,27]. In the case of MoO_3, the Mo 4d contribution in the XPS valence band spectra around the Fermi level is negligible. Further analysis of the valence band spectrum shows for the case of MoO_3 that the highest Mo 4d contribution to the occupied density of states are found in the regions labelled as I, II and III which overlap with the O 2p partial density of states seen as a broad feature at $\approx$ 6 eV. From a linear extrapolation of the valence band edge to zero, a value of = 2.9 ± 0.1 eV is calculated for the valence band onset. This value is consistent with other values reported in literature as determined by XPS and absorption measurements [26]. Further confirmation MoO_3-to-MoO_2 transformation is provided by the Mo 3d photoelectron core levels of the MoO_3 and MoO_2 films obtained after step #1 and step #3 and shown in Figure S2 and whose profiles are consistent with those provided by Scanlon et al [26].

These results are presented as proof-of-concept of the chemical mechanisms and the processing steps to be followed to attain the proposed reversible MoO_3-to-MoO_2 transformation. Further optimization of the annealing parameters is ongoing. Noteworthy, this innovative way of modulating the optical response of MoO_3-to-MoO_2 through annealing in air and H_2 has similarly been used in VO_2 as a new way to modulate its optical response [28].

3.2. Optical characterization of MoO₃ and MoO₂

Figure 2(a) shows the complex dielectric function of MoO_3 and MoO_2 extracted from spectroscopic ellipsometry measurements of the films after each step of the processing. MoO_3 has been modeled
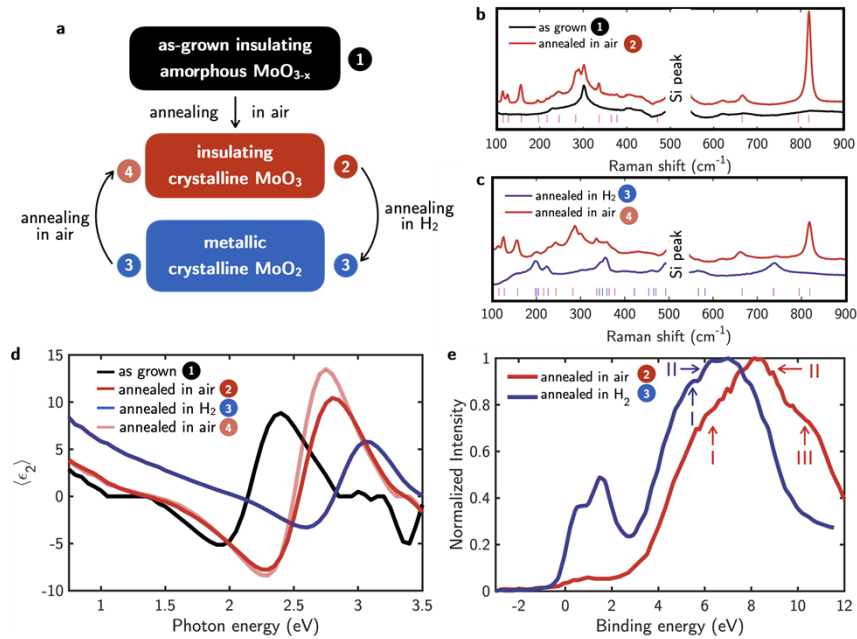
Fig. 1. (a) Sketch summarizing the path to the reversible MoO$_3$–to-MoO$_2$ transition starting from a 150 nm MoO$_{3-x}$ films on a Si substrate. (b) Raman spectra of the as-deposited MoO$_{3-x}$ before (step #1) and after annealing in air (step #2). With vertical red lines are indicated the MoO$_3$ Raman modes. (c) Raman spectra of the film annealed in H$_2$ (step #3) and subsequent annealing in air (step #4). With vertical red and blue lines are indicated the MoO$_3$ and MoO$_2$ Raman modes. (d) Imaginary part, $\langle \epsilon_2 \rangle$, of the pseudodielectric function ($\langle \epsilon \rangle = \langle \epsilon_1 \rangle + i \langle \epsilon_2 \rangle$) at each step (from #1 to #4) of the annealing of the MoO$_x$ films of 150 nm deposited on Si. (e) XPS valence band spectra of the MoO$_{3-x}$ film after annealing in air (step #2) and of the film annealed in H$_2$ (step #3).

using a Tauc-Lorentz dispersion that allow us to stablish its energy band gap at $E_g = 2.7 \pm 0.1$ eV, in agreement with its semiconducting behavior. This value is consistent with the valence band onset calculated from the XPS measurements. In the case of MoO$_2$, the dielectric function shows strong absorption below 3.0 eV consistent with measurements reported by Chase [29] and associated to quasiparticle absorption resulting from the alteration of the density of states by electronic correlation. The dielectric function has been modeled using a Tauc-Lorentz dispersion with a Drude component to model the metallic behavior at low photon energies. The Drude is justified by the appearance of metallic states around the Fermi level after annealing in H$_2$ as shown in the XPS valence band spectra in Fig. 1(e).

The MoO$_3$-to-MoO$_2$ refractive index contrast, defined as $\Delta n = n_{\text{insulating}} - n_{\text{metallic}}$ and $\Delta k = k_{\text{insulating}} - k_{\text{metallic}}$, has been presented as a key metric to evaluate the performance of a material for its application in reconfigurable photonics [30]. The values of Δk are related with different light absorption between metallic and insulating phases (amplitude modulation), whereas Δn is related to the difference in phase shifts (phase modulation). The spectral value of Δn and Δk for MoO$_x$ is shown in Fig. 2(b) compared also to the value for VO$_2$ as Ref. [2]. The spectral values of $|\Delta k|$ are demonstrated to be higher for MoO$_x$ above 1 eV with the additional advantage that the insulating phase MoO$_3$ is loss-less as opposed to the lossy behavior of both metallic and insulating VO$_2$. Contrarily, for $|\Delta n|$ the values of MoO$_x$ are almost constant ($|\Delta n| \approx 0.50$-0-75) all over the visible range whereas for VO$_2$ it takes higher and increasing values with decreasing photon energy ($|\Delta n| \approx 0.5$-1.4). Therefore, considering these results, MoO$_x$ is a
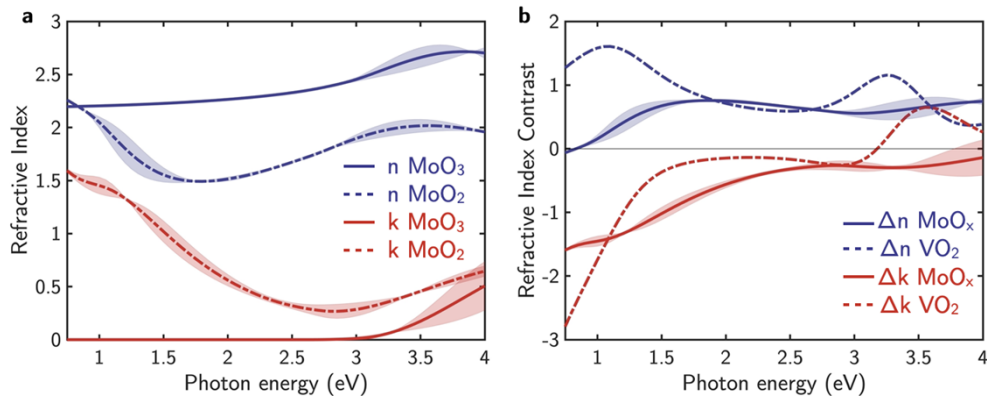
Fig. 2. (a) Refractive index of MoO_3 and MoO_2 as extracted from the ellipsometry fitting. (b) Refractive index contrast between MoO_3 and MoO_2. As reference, it is also shown the refractive index contrast of VO_2.

promising material to be integrated in photonic devices for amplitude modulation purposes in the visible and near IR considering its high values of Δk being one of the phases loss-less (i.e., MoO_3). For VO_2, a similar type of behavior is obtained in the infrared in 2 μm–10 μm range where $k_{insulating} \approx 0.07$ and $k_{metallic} = 5$ - 10.

3.3. Reflectance modulation in MoO_x thin films

A thin-film material with adjustable complex permittivity can be considered as the simplest configuration to attain amplitude and phase modulators. Therefore, reflectance measurements taken at a 70° angle of incidence using unpolarized light on MoO_x films deposited on Si and Pt substrates are shown in Figs. 3(a, c) at each step of the MoO_3-to-MoO_2 transition showing the good reversibility of the optical response of the films over a full cycle. For the film deposited on Si, Fig. 3(a) shows the initial reflectance spectrum in the MoO_3 state shows a dip at 1.35 eV, which is well reversible and reproducible upon a full switching cycle, while the MoO_2 reflectance at that photon energy is almost constant at approximately $R = 0.38$. Upon transformation from MoO_3 to MoO_2, the dip in the reflectance spectrum shifts to 2.25 eV where the reflectance of MoO_3 takes a constant value of $R = 0.37$. Thus, through the MoO_3-to-MoO_2 transition, reflectance can be modulated at the two photon energies of 1.35 eV and 2.25 eV simultaneously, with $\Delta R = 0.35$ and $\Delta R = 0.27$ respectively. Figure 3(b) shows that the shift in the dip in the reflectance spectra is again well reproduced by simulated values of the reflectance using the transfer matrix method in a multilayer model that mimics the experimental conditions (see inset in Fig. 3(b)) and using the extracted dielectric functions in Fig. 2(a). Parallel measurements and simulations were run over a system consisting of a MoO_x films on a Pt substrate. Figure 3(c) shows the MoO_3 reflectance spectrum with two dips at 0.8 and 2.3 eV, which are also well reproducible upon a full transformation cycle. The line shape and dips of the experimental spectra are well reproduced by the simulated spectra in Fig. 3(d) using the transfer matrix method in a multilayer model that mimics the experimental conditions (see inset in Fig. 3(d)) and using the extracted dielectric functions in Fig. 2(a). The slight differences in the amplitude between the simulated and experimental reflectance spectra in Figs. 3(b, d) could be attributed to surface roughness effects of samples, which scatter light in a different direction from the specular one and that are not considered in the calculation.

The metal (MoO_2)-to-insulating (MoO_3) behavior in molybdenum oxide has been recently proposed as the base for a new generation of reflective displays [19]. The reflective color can be calculated by converting reflectance spectra of the films to color coordinates using color
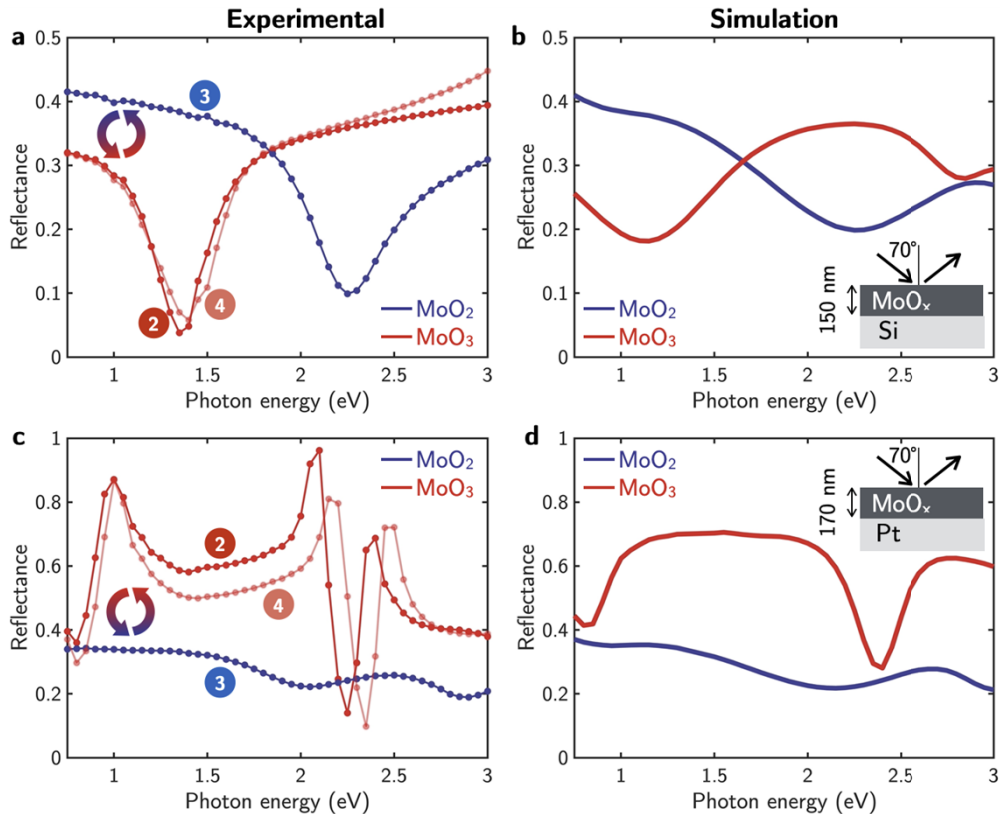
Fig. 3. Reflectance (a,c) measurements and (b,d) simulation of a MoO_3-to-MoO_2 reversible cycle for the configurations sketched in (b) ad (d) and consisting of 150 nm and 170 nm MoO_x thin films on Si and Pt, respectively, illuminated at 70° angle of incidence.

matching functions. Figure 4 shows the color calculated using the experimental and simulated reflectance spectra in Fig. 3. In order to evaluate the reproducibility of the reflective color over the completion of a full cycle, the color difference, ΔE, between calculated colors from the experimental reflectance spectra at the beginning (step #2) and at the end (step #4) of the processing of the films were obtained following Eq. (1). This magnitude is defined as the Euclidian distance between the color coordinates of each state in the *Lab* color space. Only color differences $\Delta E > 3$ are perceived by the human eye. The calculated color differences are very low, i.e., $\Delta E = 5.45$ and 2.63 for the film on Pt and Si substrates respectively, demonstrating the good reproducibility of the reflective color over a full MoO_3-to-MoO_2 transformation cycle independently of the substrate. Noteworthy, there is also a good agreement between the color calculated from the experimental and simulated reflectance spectra. The color differences between experimental and simulated color are $\Delta E = 24.65$ and 9.55 for MoO_3 (step #2 and #4) on Si and Pt substrates. For MoO_2 (step #3), the color differences are $\Delta E = 15.2$ and 8.9 for Si and Pt substrates.

Specifically, in Ref. [19], the authors propose a system consisting of MoO_x on a Pt mirror in which "on" CMY (cyan-magenta-yellow) subtractive vivid colors are achieved using insulating MoO_3, while pale colors are obtained by metallic MoO_2. This effect is herein demonstrated in Fig. 4(b), in which for MoO_3 a pinkish vivid color is observed, while for MoO_2 the reflective color turns grey. In the HSV (hue-saturation-value) color space, the saturation value drops from
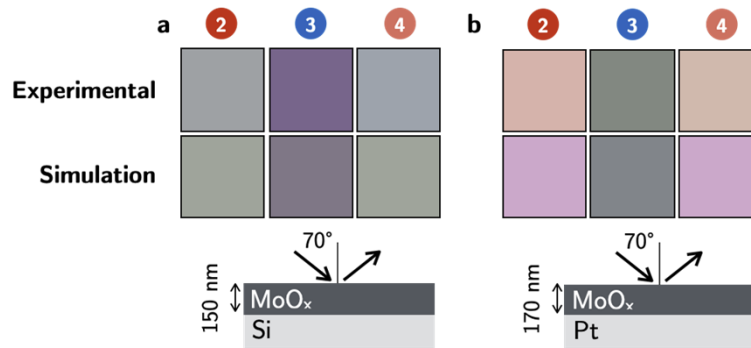
Fig. 4. Comparison between colors calculated from the experimental and simulated reflectance for the sample configuration sketched at the bottom and consisting of (a) a 150 nm MoO_x thin film on Si and (b) a 170 nm MoO_x thin film on Pt illuminated at the angle of incidence of 70°.

$S = 22$ for the "on" vivid color (i.e. MoO_3) to $S = 7$ for the "off" dull pale color (i.e. MoO_2). Interestingly, for both MoO_x on Si and MoO_x on Pt, after the completion of the cycle, we verified that the initial color of the films is recovered.

Other reconfigurable reflective displays have been proposed in literature based on the prototype phase-change material GST [31,32]. However, because both amorphous and crystalline phases present high losses optical frequencies, the change in the color present a lower contrast in luminosity and chromaticity [32]. Therefore, the advantage of MoO_x with respect to GST is that, while for one of the states a vivid color can be achieved, for the other state a low luminosity dull color can be produced. In this way, high chroma and high luminosity "on" pixel states and low chroma and low luminosity "off" pixel states can be generated. This phenomenon relies on the fact that MoO_3 is loss-less while MoO_2 is highly absorbing.

Given the good agreement between the theoretical modeling and experimental data as well as the potential of MoO_x for amplitude modulation photonic platforms, Figs. 5(a)-(c) shows the spectral value of reflectance of MoO_2 and MoO_3 as function of the molybdenum oxide layer thickness as well as the difference in reflectance, ΔR, to evaluate the potential of the insulator-to-metal transition (IMT) in light amplitude modulation schemes in the visible. In order to maximize the value of ΔR, the reflectance calculations have been performed in the configuration sketched in the inset, i.e., a MoO_x layer of variable thickness on a Pt mirror illuminated at normal incidence, yielding values of ΔR in the range 0.40-0.05 in the visible range (1.5 to 3 eV). This configuration has been chosen as we have verified that is experimentally feasible. Nevertheless, higher ΔR could be achieved by choosing a substrate with higher reflectivity (e.g., replacing Pt with silver, Ag, values of ΔR in the range 0.70-0.95 can be achieved, see Figure S3).

The reflectance, R, for MoO_2 decreases from 0.30 to 0.10 as the photon energy increases, while for MoO_3 R goes from approximately 0.7-0.6 to 0.4-0.5. For comparison, Figs. 5(d)-(f) shows equivalent calculations of R and ΔR for the VO_2 IMT, using the VO_2 dielectric function from Ref. [2]. In the visible, VO_2 shows values of ΔR in the 0.1-0.2 range, considerably lower than MoO_x. VO_2-based thin films configurations yields high reflectance modulations in the IR. For instance, Kats et al. [33] reported reflectivity modulation from 80% to 0.25% at $\lambda = 11.6$ µm for VO_2 on sapphire substrate, while Butakov et al. [34], reported high reflectivity modulation in the IR by Ge/VO_2/sapphire multilayer systems.

Thus, these results suggest that the MIT in MoO_x shows a better performance for light modulation in the visible than VO_2.
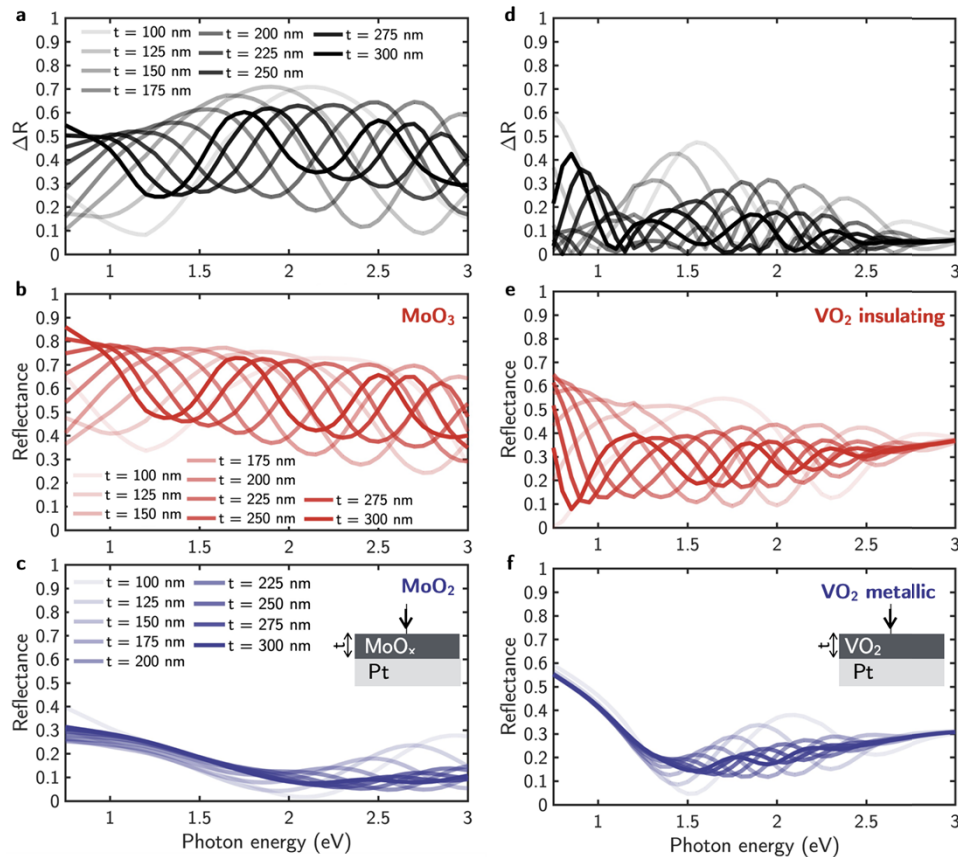
Fig. 5. Difference in reflectance, ΔR, between metallic and insulating phases of (a) MoO_x and (d) VO_2 on a Pt mirror at normal incidence as a function of the layer thickness. Reflectance, R, as a function of the layer thickness for the insulating phases (b) MoO_3 and (e) insulating VO_2. Reflectance, R, as a function of the layer thickness for the metallic phases (c) MoO_2 and (f) metallic VO_2.

3.4. Amplitude modulation in cladded Si_3N_4 waveguides

Integration of materials with reconfigurable optical response such as VO_2 or chalcogenide phase change materials (PCMs) such as GST or Sb_2S_3 in photonic integrated circuits (PICs) has led to a wide range of new functionalities ranging from programmable photonic processing, [35,36] optical memories, [37,38] optical switches [5,39] and modulators, [40–43] as well as neuromorphic computing [44]. Generally, VO_2 as well as PCMs are integrated in the PICs by depositing small patches of these materials on top of the waveguides. By triggering the IMT of VO_2 with an external excitation (i.e., heat, electric field, or light), the guided mode experiences a change in both optical phase and amplitude. For VO_2 on Si waveguide modulators, it has been pointed out that insertion loss must be carefully considered due to the non-zero imaginary part ($k \neq 0$) of the refractive index of insulating VO_2, resulting in optical absorption in the passive state of the modulator [45]. In the case of MoO_x, the insulating phase MoO_3 presents an extinction coefficient equal to zero ($k = 0$), thus, resulting in a loss-less passive state. The possibility of integrating MoO_3 into a silicon photonics platform has been recently demonstrated [46].

In order to explore the performance of MoO_x as material to be integrated in PICs for optical switching applications, we have calculated the change in transmission, ΔT, through a waveguide

as function of the length of a 20 nm thick MoO_x patch in insulating (MoO_3) and metallic states (MoO_2) deposited on top of it as sketched in Fig. 6(a). The same simulations are performed for the two phases of VO_2 (metallic and insulating). The waveguide (width = 800 nm and height = 300 nm) is made of silicon nitride (Si_3N_4) deposited on a silicon dioxide substrate (SiO_2). Transmission calculations have been performed for a wavelength of $\lambda = 1550$ nm (telecom C-band). At this wavelength, the refractive index of the waveguide and the substrate are $n = 1.99$ and $n = 1.44$ respectively. In these simulations, the fundamental electrical mode is selected for the study. As shown in Fig. 6(b), the transmission through the waveguide as function of the length of the cladding layer strongly depends on the optical properties of the cladding material (insulating or metallic VO_2 and MoO_3 or MoO_2).
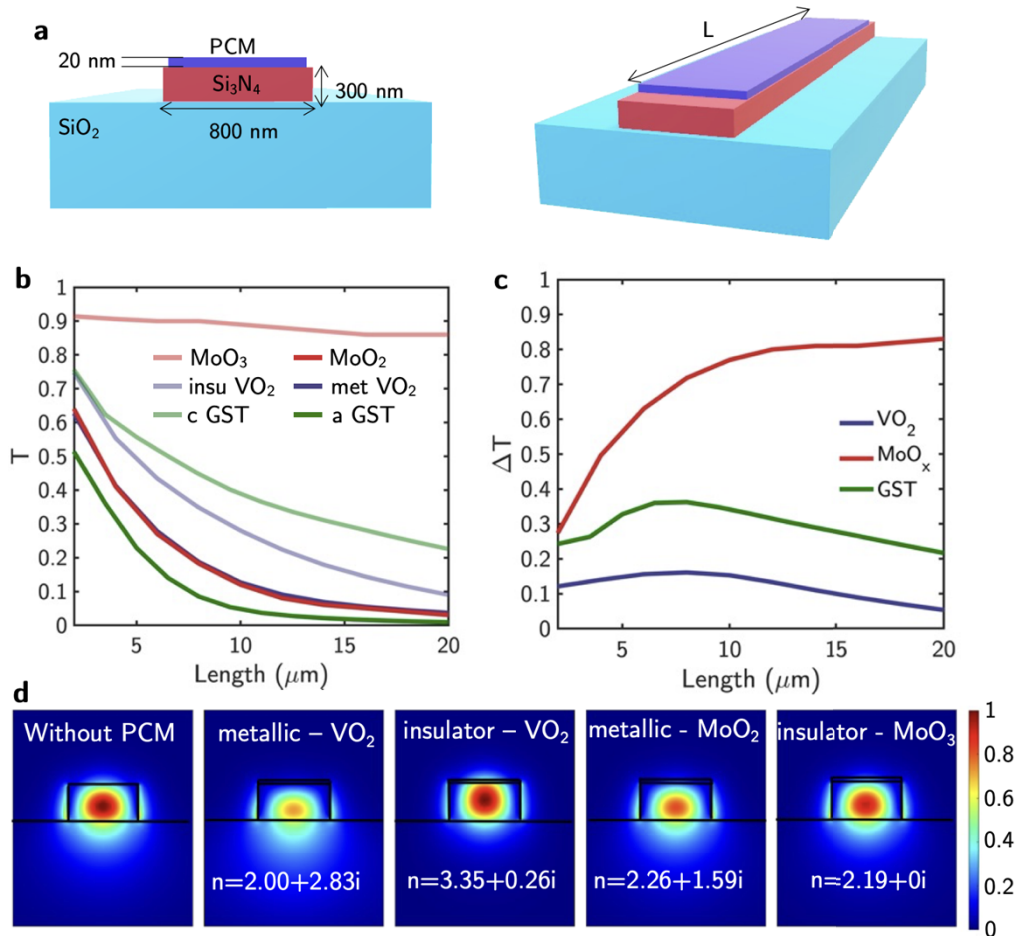
Fig. 6. (a) Scheme of the hybrid waveguide. A 20 nm thick MoO_x or VO_2 deposited on top a silicon nitride waveguide over a silicon dioxide substrate. (b) Transmission through a waveguide as a function of the length for the different phases (metallic and insolating of MoO_x and VO_2). (c) Transmission contrast between the two phases of MoO_x and VO_2 for different lengths. In (b) and (c) is included equivalent calculations for amorphous and crystalline GST as reference. (d) Mode profile of the fundamental electric mode for the different cladding materials.

The refractive indices of the four phases considered in the calculations are: $n = 2.00 + 2.83i$ (metallic VO_2), $n = 3.35 + 0.26i$ (insulating VO_2), $n = 2.26 + 1.59i$ (MoO_2) and $n = 2.19 + 0.00i$

(MoO$_3$) for the wavelength of 1550 nm. The highest transmission is obtained for MoO$_3$ as $k = 0$. Nevertheless, it presents low losses because its refractive index is slightly higher than the one of the waveguides ($n = 1.99$) and total internal reflection (TIR) inside the waveguide is not completely guaranteed. Insulating VO$_2$ results in a lower transmission than MoO$_3$ because of its extinction coefficient $k = 0.26$ and its real part much higher than the $n = 1.99$ of the Si$_3$N$_4$ waveguide. Metallic VO$_2$ and MoO$_2$ present low transmission due to its high value of the extinction coefficient, k, consistently with their metallic behavior. The transmission contrast ΔT between metallic and insulating phases of MoO$_x$ and VO$_2$ is plotted in Fig. 5(c), showing a higher contrast for MoO$_x$. Specifically, a contrast as a high as 0.8 can be obtained using MoO$_x$ as an active element in reconfigurable cladded waveguides. For comparison, in the case VO$_2$, the highest value of ΔT is 0.2, i.e., four times lower than in the case of MoO$_x$. The mode profile of the fundamental electric mode for the different phases is shown in Fig. 6(d).

As reference in Fig. 6(b), (c) is shown the data corresponding to the amorphous-to-crystalline transition of GST, as prototypical system ($n_{amorph} + ik_{amorph} = 4.352 + 0.060i$ and $n_{cryst} + ik_{cryst} = 7.912 + 1.030i$). This material shows a higher ΔT than VO$_2$, but lower than MoO$_x$. Nevertheless, it should be noted that because the switching speed for MoO$_x$ is lower and its actuation in this particular configuration is probably more complicated than for GST (annealing in different atmosphere versus only annealing/melt quench), MoO$_x$ may not competitive for its integration in reconfigurable PIC architectures as the ones proposed for GST related to programmable photonics [35,47], neuromorphic computing [44,48], non-volatile and rewritable data storage [37,49].

Conclusions

We have demonstrated the reversible non-volatile MoO$_3$-to-MoO$_2$ transition associated to change from a metallic (MoO$_2$) to a dielectric (MoO$_3$) behavior in the dielectric function. Amorphous MoO$_{x-3}$ on 4 inches silicon wafers were fabricated by e-beam deposition and subsequently crystallized into MoO$_3$ by annealing in air. MoO$_3$-to-MoO$_2$ non-volatile transition has been achieved reversibly through cycles of annealing in hydrogen and air. The analysis of the refractive index contrast between both phases and its comparison with analogous values for canonical insulating-to-metal transition material VO$_2$, reveals the superior performance of MoO$_x$ for amplitude modulation photonic platforms at the C telecom band (1550 nm) as well as for reflectivity modulators in the visible range.

Disclosures. The authors declare no conflict of interests.

Data availability. The refractive index of MoO$_2$ and MoO$_3$ are available at [50]

Supplemental document. See Supplement 1 for supporting content.

References

1. S. Cueff, J. John, Z. Zhang, J. Parra, J. Sun, R. Orobtchouk, S. Ramanathan, and P. Sanchis, "VO$_2$ nanophotonics," APL Photonics **5**(11), 110901 (2020).
2. J. John, Y. Gutierrez, Z. Zhang, H. Karl, S. Ramanathan, R. Orobtchouk, F. Moreno, and S. Cueff, "Multipolar Resonances with Designer Tunability Using VO$_2$ Phase-Change Materials," Phys. Rev. Appl. **13**(4), 044053 (2020).
3. A. Tripathi, J. John, S. Kruk, Z. Zhang, H. S. Nguyen, L. Berguiga, P. R. Romeo, R. Orobtchouk, S. Ramanathan, Y. Kivshar, and S. Cueff, "Tunable Mie-Resonant Dielectric Metasurfaces Based on VO$_2$ Phase-Transition Materials," ACS Photonics **8**(4), 1206–1213 (2021).
4. R. M. Briggs, I. M. Pryce, and H. A. Atwater, "Compact silicon photonic waveguide modulator based on the vanadium dioxide metal-insulator phase transition," Opt. Express **18**(11), 11192 (2010).
5. K. J. Miller, K. A. Hallman, R. F. Haglund, and S. M. Weiss, "Silicon waveguide optical switch with embedded phase change material," Opt. Express **25**(22), 26527 (2017).
6. I. Olivares, L. Sánchez, J. Parra, R. Larrea, A. Griol, M. Menghini, P. Homm, L.-W. Jang, B. van Bilzen, J. W. Seo, J.-P. Locquet, and P. Sanchis, "Optical switching in hybrid VO$_2$/Si waveguides thermally triggered by lateral microheaters," Opt. Express **26**(10), 12387 (2018).
7. S. Cueff, D. Li, Y. Zhou, F. J. Wong, J. A. Kurvits, S. Ramanathan, and R. Zia, "Dynamic control of light emission faster than the lifetime limit using VO$_2$ phase-change," Nat. Commun. **6**(1), 8636 (2015).

8. E. Petronijevic, M. Centini, T. Cesca, G. Mattei, F. A. Bovino, and C. Sibilia, "Control of Au nanoantenna emission enhancement of magnetic dipolar emitters by means of VO$_2$ phase change layers," Opt. Express **27**(17), 24260 (2019).

9. P. K. Jha, H. Akbari, Y. Kim, S. Biswas, and H. A. Atwater, "Nanoscale axial position and orientation measurement of hexagonal boron nitride quantum emitters using a tunable nanophotonic environment," Nanotechnology **33**(1), 015001 (2022).

10. T. He and J. Yao, "Photochromism of molybdenum oxide," J. Photochem. Photobiol., C **4**(2), 125–143 (2003).

11. G. Álvarez-Pérez, T. G. Folland, I. Errea, J. Taboada-Gutiérrez, J. Duan, J. Martín-Sánchez, A. I. F. Tresguerres-Mata, J. R. Matson, A. Bylinkin, M. He, W. Ma, Q. Bao, J. I. Martín, J. D. Caldwell, A. Y. Nikitin, and P. Alonso-González, "Infrared Permittivity of the Biaxial van der Waals Semiconductor α-MoO$_3$ from Near- and Far-Field Correlative Studies," Adv. Mater. **32**(29), 1908176 (2020).

12. M. Chen, X. Lin, T. H. Dinh, Z. Zheng, J. Shen, Q. Ma, H. Chen, P. Jarillo-Herrero, and S. Dai, "Configurable phonon polaritons in twisted α-MoO$_3$," Nat. Mater. **19**(12), 1307–1311 (2020).

13. Q. Zhang, X. Li, Q. Ma, Q. Zhang, H. Bai, W. Yi, J. Liu, J. Han, and G. Xi, "A metallic molybdenum dioxide with high stability for surface enhanced Raman spectroscopy," Nat. Commun. **8**(1), 14903 (2017).

14. Y. Zhan, Y. Liu, H. Zu, Y. Guo, S. Wu, H. Yang, Z. Liu, B. Lei, J. Zhuang, X. Zhang, D. Huang, and C. Hu, "Phase-controlled synthesis of molybdenum oxide nanoparticles for surface enhanced Raman scattering and photothermal therapy," Nanoscale **10**(13), 5997–6004 (2018).

15. W. Lee, C. J. Cho, W. C. Lee, C. S. Hwang, R. P. H. Chang, and S. K. Kim, "MoO$_2$ as a thermally stable oxide electrode for dynamic random-access memory capacitors," J. Mater. Chem. C **6**(48), 13250–13256 (2018).

16. Y. Shi, B. Guo, S. A. Corr, Q. Shi, Y.-S. Hu, K. R. Heier, L. Chen, R. Seshadri, and G. D. Stucky, "Ordered Mesoporous Metallic MoO$_2$ Materials with Highly Reversible Lithium Storage Capacity," Nano Lett. **9**(12), 4215–4220 (2009).

17. B. Guo, X. Fang, B. Li, Y. Shi, C. Ouyang, Y.-S. Hu, Z. Wang, G. D. Stucky, and L. Chen, "Synthesis and Lithium Storage Mechanism of Ultrafine MoO$_2$ Nanorods," Chem. Mater. **24**(3), 457–463 (2012).

18. L. C. Yang, Q. S. Gao, Y. Tang, Y. P. Wu, and R. Holze, "MoO$_2$ synthesized by reduction of MoO$_3$ with ethanol vapor as an anode material with good rate capability for the lithium ion battery," J. Power Sources **179**(1), 357–360 (2008).

19. G. Santos, F. Gonzalez, D. Ortiz, J. M. Saiz, M. Losurdo, F. Moreno, and Y. Gutierrez, "Dynamic reflective color pixels based on molybdenum oxide," Opt. Express **29**(13), 19417 (2021).

20. G. Santos, F. González, D. Ortiz, J. M. Saiz, M. Losurdo, Y. Gutiérrez, and F. Moreno, "Design of Switchable On/Off Subpixels for Primary Color Generation Based on Molybdenum Oxide Gratings," Physics **3**(3), 655–663 (2021).

21. G. E. Jellison and F. A. Modine, "Parameterization of the optical functions of amorphous materials in the interband region," Appl. Phys. Lett. **69**(3), 371–373 (1996).

22. M. Born, E. Wolf, A. B. Bhatia, P. C. Clemmow, D. Gabor, A. R. Stokes, A. M. Taylor, P. A. Wayman, and W. L. Wilcock, *Principles of Optics* (Cambridge University Press, 1999).

23. J. Schanda, *Colorimetry: Understanding the CIE System* (John Wiley & Sons, Inc., 2007).

24. M. Dieterle and G. Mestl, "Raman spectroscopy of molybdenum oxides," Phys. Chem. Chem. Phys. **4**(5), 822–826 (2002).

25. M. A. Camacho-López, L. Escobar-Alarcón, M. Picquart, R. Arroyo, G. Córdoba, and E. Haro-Poniatowski, "Micro-Raman study of the m-MoO$_2$ to α- MoO$_3$ transformation induced by cw-laser irradiation," Opt. Mater. **33**(3), 480–484 (2011).

26. D. O. Scanlon, G. W. Watson, D. J. Payne, G. R. Atkinson, R. G. Egdell, and D. S. L. Law, "Theoretical and Experimental Study of the Electronic Structures of MoO$_3$ and MoO$_2$," J. Phys. Chem. C **114**(10), 4636–4645 (2010).

27. V. Eyert, R. Horny, K.-H. Höck, and S. Horn, "Embedded Peierls instability and the electronic structure of MoO$_2$," J. Phys.: Condens. Matter **12**(23), 4923–4946 (2000).

28. X. Duan, S. T. White, Y. Cui, F. Neubrech, Y. Gao, R. F. Haglund, and N. Liu, "Reconfigurable Multistate Optical Systems Enabled by VO$_2$ Phase Transitions," ACS Photonics **7**(11), 2958–2965 (2020).

29. L. L. Chase, "Optical properties of CrO$_2$ and MoO$_2$ from 0.1 to 6 eV," Phys. Rev. B **10**(6), 2226–2231 (1974).

30. S. Abdollahramezani, O. Hemmatyar, H. Taghinejad, A. Krasnok, Y. Kiarashinejad, M. Zandehshahvar, A. Alu, and A. Adibi, "Tunable nanophotonics enabled by chalcogenide phase-change materials," Nanophotonics **9**(5), 1189–1241 (2020).

31. P. Hosseini, C. D. Wright, and H. Bhaskaran, "An optoelectronic framework enabled by low-dimensional phase-change films," Nature **511**(7508), 206–211 (2014).

32. B. Broughton, L. Bandhu, C. Talagrand, S. Garcia-Castillo, M. Yang, H. Bhaskaran, and P. Hosseini, "38-4: Solid-State Reflective Displays (SRD ®) Utilizing Ultrathin Phase-Change Materials," SID Symp. Dig. Tech. Pap. **48**(1), 546–549 (2017).

33. M. A. Kats, D. Sharma, J. Lin, P. Genevet, R. Blanchard, Z. Yang, M. M. Qazilbash, D. N. Basov, S. Ramanathan, and F. Capasso, "Ultra-thin perfect absorber employing a tunable phase change material," Appl. Phys. Lett. **101**(22), 221101 (2012).

34. N. A. Butakov, M. W. Knight, T. Lewi, P. P. Iyer, D. Higgs, H. T. Chorsi, J. Trastoy, J. Del Valle Granda, I. Valmianski, C. Urban, Y. Kalcheim, P. Y. Wang, P. W. C. Hon, I. K. Schuller, and J. A. Schuller, "Broadband Electrically Tunable Dielectric Resonators Using Metal–Insulator Transitions," ACS Photonics **5**(10), 4056–4060 (2018).

35. M. Stegmaier, C. Ríos, H. Bhaskaran, C. D. Wright, and W. H. P. Pernice, "Nonvolatile All-Optical 1 × 2 Switch for Chipscale Photonic Networks," Adv. Opt. Mater. **5**(1), 1600346 (2017).

36. M. Delaney, I. Zeimpekis, D. Lawson, D. W. Hewak, and O. L. Muskens, "A New Family of Ultralow Loss Reversible Phase-Change Materials for Photonic Integrated Circuits: Sb_2S_3 and Sb_2Se_3," Adv. Funct. Mater. **30**(36), 2002447 (2020).

37. C. Ríos, M. Stegmaier, P. Hosseini, D. Wang, T. Scherer, C. D. Wright, H. Bhaskaran, and W. H. P. Pernice, "Integrated all-photonic non-volatile multi-level memory," Nat. Photonics **9**(11), 725–732 (2015).

38. Y. Jung, H. Han, A. Sharma, J. Jeong, S. S. P. Parkin, and J. K. S. Poon, "Integrated Hybrid VO_2 –Silicon Optical Memory," ACS Photonics **9**(1), 217–223 (2022).

39. A. Joushaghani, J. Jeong, S. Paradis, D. Alain, J. Stewart Aitchison, and J. K. S. Poon, "Wavelength-size hybrid Si-VO_2 waveguide electroabsorption optical switches and photodetectors," Opt. Express **23**(3), 3657 (2015).

40. H. M. K. Wong, Z. Yan, K. A. Hallman, R. E. Marvel, R. P. Prasankumar, R. F. Haglund, and A. S. Helmy, "Broadband, Integrated, Micron-Scale, All-Optical Si_3N_4/VO_2 Modulators with pJ Switching Energy," ACS Photonics **6**(11), 2734–2740 (2019).

41. V. Jeyaselvan, A. Pal, P. S. Anil Kumar, and S. K. Selvaraja, "Thermally-induced optical modulation in a vanadium dioxide-on-silicon waveguide," OSA Continuum **3**(1), 132 (2020).

42. Y. Gutiérrez, A. P. Ovvyan, G. Santos, D. Juan, S. A. Rosales, J. Junquera, P. García-Fernández, S. Dicorato, M. M. Giangregorio, E. Dilonardo, F. Palumbo, M. Modreanu, J. Resl, O. Ishchenko, G. Garry, T. Jonuzi, M. Georghe, C. Cobianu, K. Hingerl, C. Cobet, F. Moreno, W. H. P. Pernice, and M. Losurdo, "Interlaboratory study on Sb_2S_3 interplay between structure, dielectric function, and amorphous-to-crystalline phase change for photonics," iScience **25**(6), 104377 (2022).

43. J. Faneca, I. Zeimpekis, S. T. Ilie, T. D. Bucio, K. Grabska, D. W. Hewak, and F. Y. Gardes, "Towards low loss non-volatile phase change materials in mid index waveguides," Neuromorph. Comput. Eng. **1**(1), 014004 (2021).

44. J. Feldmann, N. Youngblood, C. D. Wright, H. Bhaskaran, and W. H. P. Pernice, "All-optical spiking neurosynaptic networks with self-learning capabilities," Nature **569**(7755), 208–214 (2019).

45. K. J. Miller, R. F. Haglund, and S. M. Weiss, "Optical phase change materials in integrated silicon photonic devices: review," Opt. Mater. Express **8**(8), 2415 (2018).

46. G. Ren, B. Y. Zhang, A. Mitchell, and J. Z. Ou, "A Novel 2D Plasmonic MoO_3 Driven pH Sensor on Silicon Photonics Platform," in *2019 Photonics & Electromagnetics Research Symposium - Fall (PIERS - Fall)* (IEEE, 2019), pp. 2544–2555.

47. M. Delaney, I. Zeimpekis, H. Du, X. Yan, M. Banakar, D. J. Thomson, D. W. Hewak, and O. L. Muskens, "Nonvolatile programmable silicon photonics using an ultralow-loss Sb_2Se_3, phase change material," Sci. Adv. **7**(25), 1 (2021).

48. X. Chen, Y. Xue, Y. Sun, J. Shen, S. Song, M. Zhu, Z. Song, Z. Cheng, and P. Zhou, "Neuromorphic Photonic Memory Devices Using Ultrafast, Non-volatile Phase-change Materials," Adv. Mater. 2203909 (2022).

49. M. Wuttig and N. Yamada, "Phase-change materials for rewriteable data storage," Nat. Mater. **6**(11), 824–832 (2007).

50. Y. Gutierrez, G. Santos, F. Palumbo, M. Modreanu, F. Moreno, and M. Losurdo, "Data Set-Optical Properties of MoO_3 and MoO_2," Zenodo, 2022, https://zenodo.org/record/6592425.